ACS APPLIED NANO MATERIALS

www.acsanm.org Article

Infection Microenvironment-Mediated Nanoplatform for *In Vivo* Persistent Luminescence Imaging and Chemodynamic Antibacterial Therapy

Li-Ya Wang, Li-Jian Chen, Xu Zhao, Yan Lv, Tianxi Liu, and Xiu-Ping Yan*

Cite This: *ACS Appl. Nano Mater.* 2023, 6, 2274−2283 Read Online

ACCESS | Metrics & More | Article Recommendations | Supporting Information

ABSTRACT: Infection microenvironment-mediated chemodynamic therapy (CDT) is an attractive way for the therapy of bacterial infection. However, therapeutic agents which can obtain real-time and *in situ* pathological information imaging signals during CDT are rare. Thus, it is an urgent need to explore antibacterial agents with both bacterial elimination and treatment process monitoring ability. Herein, we report an activatable antimicrobial nanoplatform with both ultralow-background persistent luminescent (PL) "turn-on" imaging and therapeutic capability. Chitosan (CS) is used as a linker to immobilize copper ions on the surface of persistent luminescent nanoparticles (PLNPs) to fabricate PLNPs−CS−Cu^{2+}. The PL emission of PLNPs is quenched by Cu^{2+} under physiological conditions but recovered due to the conversion of Cu^{2+} into Cu^{+} by high glutathione (GSH) levels at the infection site. The produced Cu^{+} catalyzes H_2O_2 to generate hydroxyl radicals ($^{\bullet}OH$) for bacterial killing through oxidative stress. Also, the depletion of GSH amplifies the oxidative stress and enhances the therapy efficacy. The as-prepared antibacterial nanoplatform is promising for highly sensitive persistent luminescent imaging and simultaneous treatment of bacterial infection.

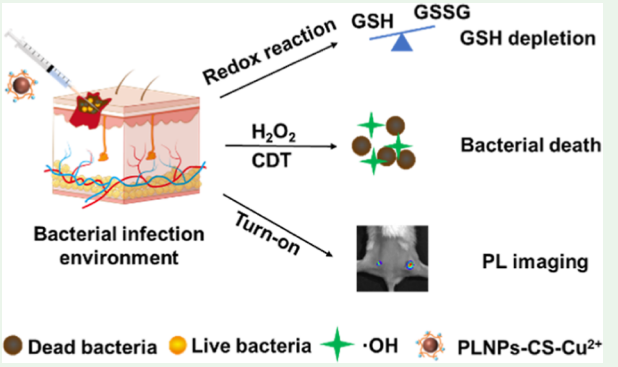

KEYWORDS: *antibacterial agent, bacterial infection, persistent luminescence imaging, chemodynamic therapy, GSH depletion*

INTRODUCTION

Bacterial infection has caused about one-third of global deaths.[1,2] The abuse of antibiotics is easy to induce drug resistance, leading to a serious crisis in public health.[3,4] Worse still, the exploitation of new antibiotics lags far behind the evolution of drug-resistant bacteria.[5] Hence, it is urgently needed to explore advanced antibacterial agents and robust approaches to solve this problem.[6] Recently, many nanotechnology-based antibacterial approaches have been applied for anti-infective treatment, including photothermal therapy (PTT), chemodynamic therapy (CDT), sonodynamic therapy (SDT), and photodynamic therapy (PDT).[7−11] CDT is a promising antibacterial approach due to high therapeutic specificity and low invasiveness.[12−14] It can *in situ* convert intracellular H_2O_2 to highly cytotoxic hydroxyl radicals ($^{\bullet}OH$) *via* Fenton-like reaction.[15,16] Recently, CDT activated by the infection microenvironment has achieved great progress in the treatment of bacterial infections.[17−19]

Several transition metals (Fe, Cu, Mn, and Co) have shown excellent Fenton-like catalytic activity.[20−22] Among them, Cu-based nanotherapeutic agents have attracted particular interest for their cheap, readily available, and high catalytic activity. The convertible valence (Cu^{2+} and Cu^{+}) of copper can be used to treat bacterial infection. Cu^{+} can catalyze H_2O_2 to produce cytotoxic $^{\bullet}OH$ to kill bacteria, while Cu^{2+} can consume the glutathione (GSH) which can scavenge the produced $^{\bullet}OH$.[23−25] This helps to aggravate $^{\bullet}OH$-induced oxidative stress and amplify therapeutic efficiency. In addition, copper ions can be antimicrobial by disrupting the respiratory chain and gene replication in bacteria and enhance the wound healing process by stimulating cell migration, collagen deposition, angiogenesis.[26,27] Nevertheless, copper ions cannot be applied directly because excessive free copper can result in serious systemic toxicity (neurodegenerative disorders, spasms, and even death).[28,29] The formation of Cu complexes can prevent the formation of free Cu^{2+} in circulation. Chitosan (CS) is a powerful chelating agent, and the availability of amino ($-NH_2$) and hydroxyl (−OH) groups enables CS to coordinate copper ions.[30,31] Thus, chitosan−copper (CS−Cu^{2+}) complexes are promising antimicrobial agents for biological applications.[32−35]

Received: January 8, 2023
Accepted: January 18, 2023
Published: January 26, 2023

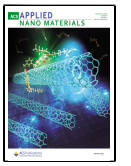

https://doi.org/10.1021/acsanm.3c00101
ACS Appl. Nano Mater. 2023, 6, 2274−2283

Scheme 1. Illustration for the Preparation of the PLNPs−CS−Cu^{2+} Nanoplatform for *In Vivo* Treating Bacterial Infection

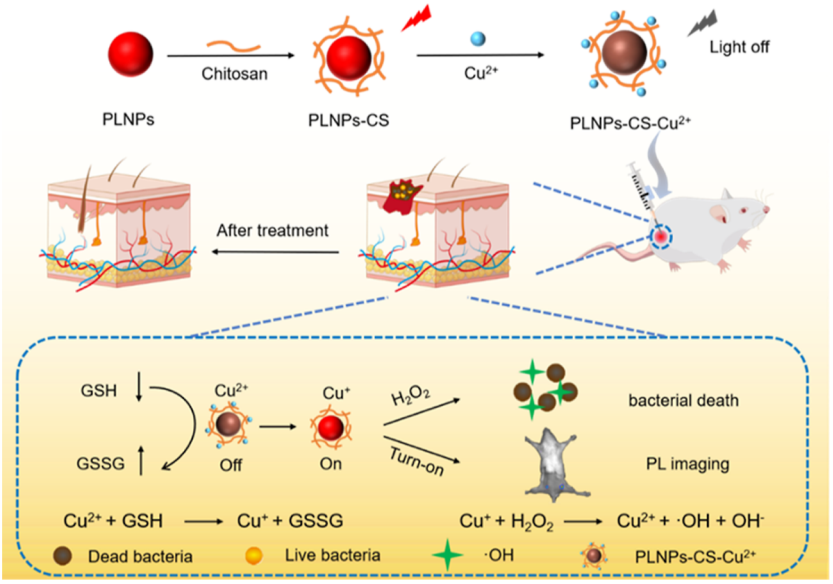

Real-time and *in situ* pathological information of bacterial infection is of paramount importance for the treatment of bacterial infection. Theranostic agents integrating imaging and therapeutic functions emerge as a potential direction for the detection and therapy of bacterial infection.[36−38] Persistent luminescent nanoparticles (PLNPs) are fascinating optical imaging materials that can emit long-lasting luminescence after ceasing excitation.[39] Such a unique property permits autofluorescence-free persistent luminescent (PL) imaging with no need for *in situ* excitation.[40,41] More importantly, Cr^{3+}-doped near-infrared (NIR) PLNPs can offer deep tissue penetration and are re-activated by red LED light, making them ideal for bacterial infection imaging in deep tissue.[42,43] Conventional PLNP-based phototherapeutic agents are mostly "always on", which reduces the sensitivity of imaging to a certain extent.[44] In contrast, activatable probes keep imaging off until they reach the site of the lesion, improving the target-to-background ratio and sensitivity. Copper ions as the significant quenchers of phosphors can endow the switch signal of PLNPs simply and directly.[45]

In this work, we show a new activatable multifunctional antibacterial nanoplatform for "turn-on" PL imaging and CDT killing of bacterial infection *in vivo*. PLNPs ($Zn_{1.25}Ga_{1.5}Ge_{0.25}O_4$:0.5% Cr^{3+}, 2.5% Yb^{3+}, and 0.25% Er^{3+}) are used as the imaging unit which can emit renewable NIR-PL under red LED illumination.[46] Then, PLNPs are surface-modified with CS to improve biocompatibility, provide rich functional groups for subsequent copper ion immobilization, and reduce the toxicity of free copper ions. Finally, copper ions are introduced onto the surface of the CS-functionalized PLNPs (PLNPs−CS) by complexation to obtain Cu^{2+}-immobilized PLNPs−CS (PLNPs−CS−Cu^{2+}). The PL of PLNPs is quenched by Cu^{2+} but rapidly recovered for the conversion of Cu^{2+} into Cu^{+} by abnormally high GSH in the infection site.[47−50] The produced Cu^{+} catalyzes H_2O_2 to generate $^{\bullet}OH$ for bacterial killing through oxidative stress. At the same time, the depletion of GSH can amplify oxidative stress and enhance the CDT therapeutic efficiency of Cu^{+}. The as-prepared PLNPs−CS−Cu^{2+} multifunctional nanoplatform is promising for sensitive imaging and treatment of bacterial infection.

EXPERIMENTAL SECTION

Synthesis of PLNPs−CS−Cu^{2+}. The PLNPs and carboxyl-modified PLNPs (PLNPs−COOH) were prepared according to previous literature studies.[46,51] PLNPs−COOH (50 mg) in 10 mM phosphate-buffered saline (PBS, pH 6) was mixed with 80 mg of EDC·HCl and 100 mg of NHS for 2 h activation. Chitosan hydrochloride (500 mg) was then added, and 12 h room temperature stirring was applied. Finally, the produced PLNPs−CS was collected *via* centrifugation.

To fabricate PLNPs−CS−Cu^{2+}, different concentrations of $CuCl_2\cdot 2H_2O$ solution were added into the solution containing PLNPs−CS (0.5 mg mL^{-1}) under constant stirring at 40 °C for various reaction times. After three times washing with pure water, the final product was collected through centrifugation. The reaction time and the concentration of $CuCl_2\cdot 2H_2O$ were optimized to be 4 h and 600 μM, respectively.

Bacterial Culture and *In Vitro* Antibacterial Experiments. A spread plate approach was employed to evaluate the antibacterial ability of PLNPs−CS−Cu^{2+} to *Staphylococcus aureus* (*S. aureus*, G^{+}). After being cultured in 5 mL of liquid LB and shaken at 37 °C for 12 h, the bacterial solution was diluted to 10^9 CFU mL^{-1} with PBS for further antibacterial assay. The bacterial suspension (100 μL) was treated under various conditions for 2 h of coincubation: (1) PBS (10 mM, pH 7.4), (2) H_2O_2 (1 mM), (3) PLNPs−CS−Cu^{2+} (200 μg mL^{-1}), and (4) PLNPs−CS−Cu^{2+} (200 μg mL^{-1}) + H_2O_2 (1 mM). After dilution with PBS, 100 μL of bacterial suspension was spread on a solid medium for 18 h incubation at 37 °C. Finally, the bacterial colonies on the plate were counted.

Animal Model. Female BALB/c mice (5−6 weeks) (Changzhou Cavens Laboratory Animal Co., Changzhou, China) were used in this work. All animal experiments were approved by the Animal Ethics Committee of Jiangnan University (JN. no 20211215b0250120[536]). The *S. aureus*-infected mouse model was built for *in vivo* PL imaging and to evaluate the therapy efficacy of PLNPs−CS−Cu^{2+}. Briefly, *S. aureus* (10^8 CFU mL^{-1}, 100 μL) was inoculated on the shaved back through subcutaneous injection. After 24 h, subcutaneous abscesses were formed on the mice.

***In Vivo* Luminescence Imaging of *S. aureus*-Infected Mice.** The potential of PLNPs−CS−Cu^{2+} for in vivo PL imaging was evaluated by injecting PLNPs−CS−Cu^{2+} (100 μL, 200 μg mL^{-1}) into subcutaneously infected and non-infected areas of the same mouse. The mice were then irradiated by a 650 nm LED light (5000 lm) for 2 min, and the PL images were acquired at different time points (5, 20, 40, and 60 min) on the IVIS imaging system.

https://doi.org/10.1021/acsanm.3c00101
ACS Appl. Nano Mater. 2023, 6, 2274−2283

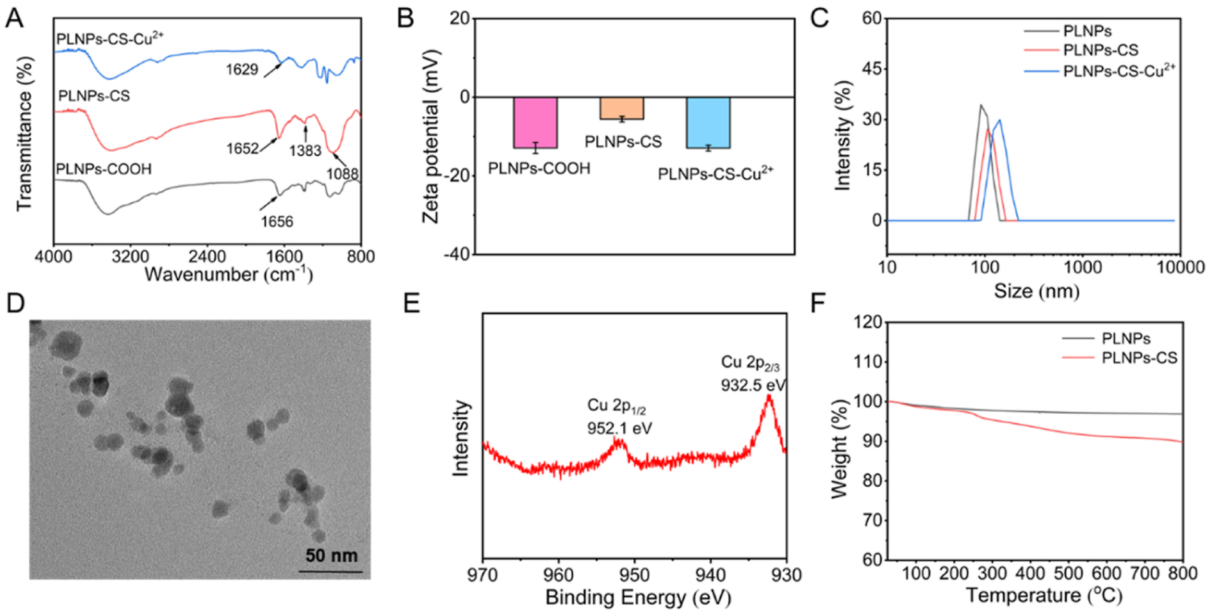

Figure 1. (A) FT-IR spectra of PLNPs, PLNPs−CS, and PLNPs−CS−Cu^{2+}. (B) Zeta potential of PLNPs, PLNPs−CS, and PLNPs−CS−Cu^{2+}. Data were presented as the mean ± SD ($n = 3$). (C) Hydrodynamic diameter distribution of PLNPs, PLNPs−CS, and PLNPs−CS−Cu^{2+}. (D) TEM images of PLNPs−CS (scale bar, 50 nm). (E) High-resolution XPS spectra of Cu 2p. (F) TGA curve of PLNPs and PLNPs−CS.

***In Vivo* Antibacterial Therapy.** The *S. aureus*-infected mice were divided into four groups randomly, and each group contained five mice. The four groups of mice were treated by direct injecting 50 μL of PBS, H_2O_2 (1 mM), PLNPs−CS−Cu^{2+} (200 μg mL^{-1}), and PLNPs−CS−Cu^{2+} + H_2O_2 into the infected abscess. The photographs of the abscesses on the mice and the mouse weights were recorded every day. Eleven days later, all the mice were immolated, and their skin tissues and major organs were excised and stained with hematoxylin and eosin (H&E) and Masson staining for histology analysis. The immunohistochemistry staining was employed to assess the expression of proinflammatory cytokines such as interleukin-6 (IL-6) and tumor necrosis factor-α (TNF-α). The suspension of the bacteria from the skin tissues was spread on solid media and incubated at 37 °C for 24 h to measure the relative bacterial viability.

RESULTS AND DISCUSSION

Design and Characterization of PLNPs−CS−Cu^{2+}. The design and fabrication of the multifunctional nanoplatform PLNPs−CS−Cu^{2+} are illustrated in Scheme 1. PLNPs ($Zn_{1.25}Ga_{1.5}Ge_{0.25}O_4$:0.5% Cr^{3+}, 2.5% Yb^{3+}, and 0.25% Er^{3+}) with superlong and reactivatable NIR-PL were used as the autofluorescence-free bioimaging unit.[46] PLNPs−CS was prepared by surface modification of the PLNPs with chitosan to improve biocompatibility and immobilize copper ions. The PLNPs−CS−Cu^{2+} nanoplatform was fabricated by further complexing Cu^{2+} with the CS of PLNPs−CS. The PL of PLNPs would be quenched after introducing Cu^{2+} but recovered when PLNPs−CS−Cu^{2+} was injected into the infection site due to the conversion Cu^{2+} to Cu^{+} by GSH. At the same time, the GSH depletion could amplify oxidative stress and enhance CDT therapeutic efficacy of Cu^{+}. Thus, the developed PLNPs−CS−Cu^{2+} nanoplatform allows the bacterial microenvironment to trigger "turn-on" imaging and enhance CDT therapeutic efficacy by GSH consumption.

The prepared PLNPs had an approximate size of 14.7 ± 3.0 nm (n = 100) (Figure S1A,B) with cubic spinel structures of Zn_2GeO_4 (JCPDS25-1018) and $ZnGa_2O_4$ (JCPDS 38-1240) (Figure S2). The successful fabrication of PLNPs−CS−Cu^{2+} was proved by Fourier transform infrared (FT-IR) spectrometry (Figure 1A). Carboxyl functionalization resulted in strong absorption bands for stretching vibration of −CO−NH− at 1656 cm^{-1}, showing the successful preparation of PLNPs−COOH. Further CS functionalization made the bands for the amidic C═O bonds stretching at 1652 cm^{-1}, the COO^- group of carboxylic acid salt at 1383 cm^{-1}, and the stretching vibration of C−O−C in the glucose unit at 1088 cm^{-1} appear,[30] confirming the formation of PLNPs−CS. The PLNPs−CS−Cu^{2+} complex was confirmed by the band position shifting to the lower wave number and changes in intensity of some bands. The newly emerged absorption band at 1629 cm^{-1} was attributed to the characteristic peak of the coordination between chitosan and Cu^{2+}.[35]

The whole functionalization process was also attested from the change in zeta potential (Figure 1B) and hydrodynamic size (Figure 1C). Modification of PLNPs−COOH with CS made the zeta potential increase from −12.9 to −5.6 mV owning to the introduced amino groups. Further complexation of Cu^{2+} made the positive charge density of chitosan decrease and the zeta potential shift to −13.0 mV. The increase in the hydrodynamic size from 97.7 nm to the final 140.2 nm revealed the successful surface modification too. Compared with PLNPs, the surface of PLNPs−CS still had uniform distribution but with an additional thin shell (Figure 1D).

The copper valence state was further confirmed by X-ray photoelectron spectroscopy (XPS) (Figure 1E). The satellite peak at 942.5 eV between the binding energies of Cu $2p_{3/2}$ (932.5 eV) and Cu $2p_{1/2}$ (952.1 eV) was ascribed to Cu^{2+} in the paramagnetic chemical state.[23,52] The amounts of Cu^{2+} were measured to be 0.56 wt % by inductively coupled plasma optical emission spectrometry (ICP-OES). The mass percentage of CS was calculated to be 10.19% based on TGA curves (Figure 1F). No obvious changes in the PL intensity, hydrodynamic diameter, and FT-IR spectra of PLNPs−CS−Cu^{2+} in PBS over 2 weeks indicate the good stability of PLNPs−CS−Cu^{2+} (Figure S4).

GSH-Activated PL Imaging. The as-prepared PLNPs exhibited a 700 nm NIR emission with excellent and red LED

https://doi.org/10.1021/acsanm.3c00101
ACS Appl. Nano Mater. 2023, 6, 2274−2283

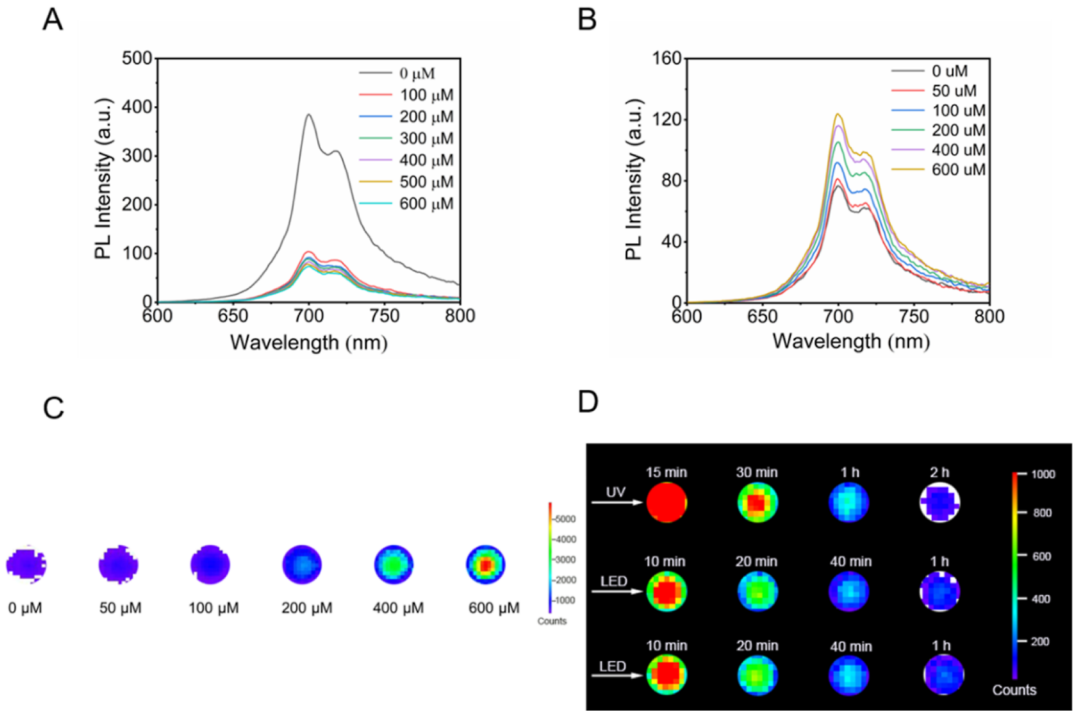

Figure 2. (A) PL intensity of PLNPs−CS reacted with various concentrations of Cu^{2+}. (B) PL intensity of PLNPs−CS−Cu^{2+} reacted with different concentrations of GSH. (C) PL images of PLNPs−CS−Cu^{2+} reacted with various concentrations of GSH. The samples were irradiated with a red LED light for 2 min. Concentration of PLNPs−CS and PLNPs−CS−Cu^{2+} for (A−C), 0.5 mg mL^{-1}. (D)LED reactivatable NIR PL images of PLNPs−CS−Cu^{+} aqueous solution (1 mg mL^{-1}) recorded on a CCD camera. The samples were pre-irradiated by a 254 nm UV lamp for 5 min, imaged at various time points after irradiation stopped, and then re-activated at 2 h with a red LED light for 2 min.

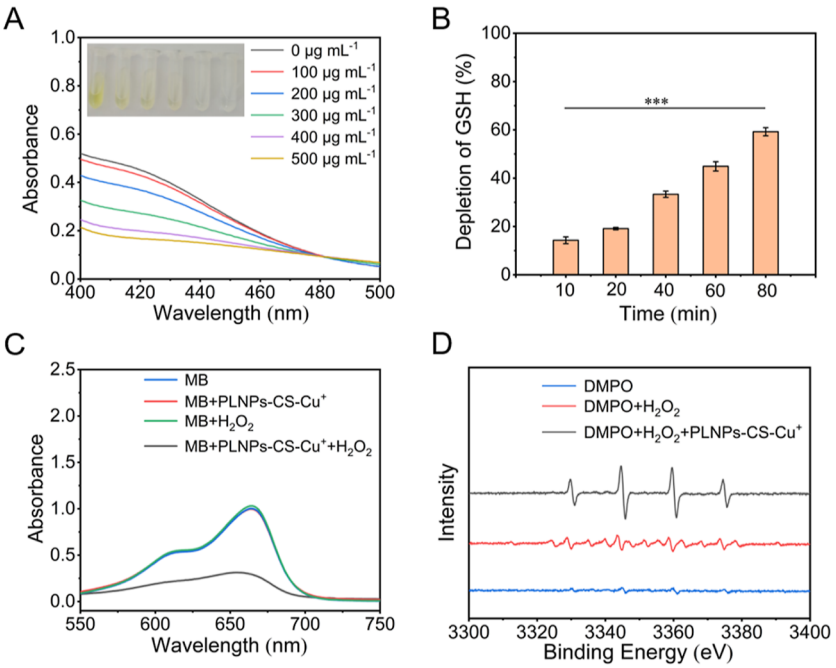

Figure 3. (A) UV−vis spectra of DTNB solutions (50 μg mL^{-1}) in the presence of GSH (500 μg mL^{-1}) and PLNPs−CS−Cu^{2+} (0−500 μg mL^{-1}). (B) GSH-depleting ability of PLNPs−CS−Cu^{2+} (500 μg mL^{-1}) in the presence of DTNB solutions (50 μg mL^{-1}) and GSH (500 μg mL^{-1}). Data were presented as mean ± SD ($n = 3$). *P* values were calculated by the Student's two-sided test (***$p < 0.001$). (C) UV−vis spectra of MB solution (10 μg mL^{-1}) after 3 h incubation in the presence of PLNPs−CS−Cu^{+}, H_2O_2, and PLNPs−CS−Cu^{+} + H_2O_2. PLNPs−CS−Cu^{+}: 0.5 mg mL^{-1} and H_2O_2: 10 mM. (D) ESR spectra for $^{\bullet}OH$ detection in the presence of DMPO, DMPO + H_2O_2, and DMPO + PLNPs−CS−Cu^{+} + H_2O_2. DMPO: 25 mM; PLNPs−CS−Cu^{+}: 1 mg mL^{-1}; and H_2O_2: 10 mM.

light reactivatable PL performance (Figure S5A−D), which makes long-term autofluorescence-free bioimaging *in vivo* available. The introduction of Cu^{2+} resulted in significant PL quenching (87.5%) of PLNPs−CS as the amount of Cu^{2+} increased (Figure 2A), while the PL intensity of PLNPs−CS−Cu^{2+} was recovered gradually as the concentration of GSH

https://doi.org/10.1021/acsanm.3c00101
ACS Appl. Nano Mater. 2023, 6, 2274−2283

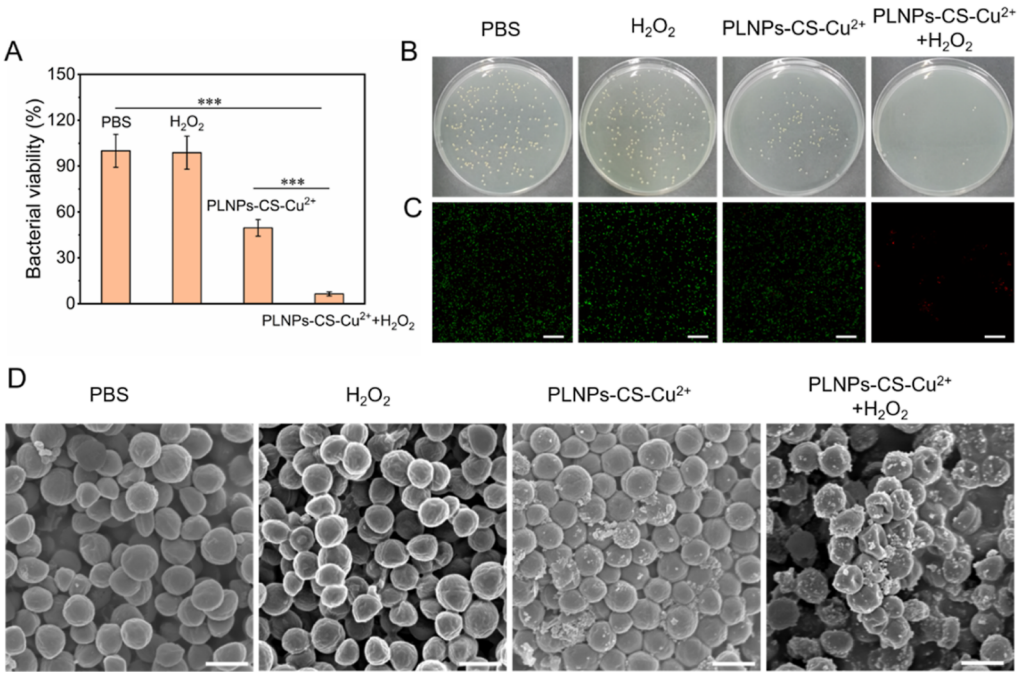

Figure 4. (A) Viability of *S. aureus* in different groups. Data were presented as the mean ± SD (n = 3). P values were calculated by the Student's two-sided test (***$p < 0.001$). (B) Agar plate photographs of the bacterial colonies in different groups. (C) Live/dead fluorescent bacterial staining of *S. aureus* in different groups. Live and dead bacteria were stained green and red, respectively (scale bar, 30 μm). (D) SEM images of different groups of bacteria (scale bar, 10 μm).

increased (Figure 2B). Similar results were also seen from the CCD images (Figure 2C). The IVIS imaging system recorded the PL signal change in PLNPs−CS−Cu^{+} over time (Figure 2D). Thus, the overexpressed GSH in the inflammatory microenvironment could make the PL of the PLNPs−CS−Cu^{2+} recover and reduce the background signal.

Consumption of GSH. GSH can prevent the oxidative stress-induced damage of cellular components, so it plays a crucial role in the bacterial antioxidant defense system. Here, the PLNPs−CS−Cu^{2+}-induced GSH consumption was evaluated by the Ellman assay.[53] In this process, colorless DTNB (5,5′-dithiobis-(2-nitrobenzoic acid)) was reduced by GSH to generate a yellow product that had a characteristic absorption peak at 412 nm. The absorbance at 412 nm decreased, and the color of the solution gradually changed from yellow to clear as the concentration of PLNPs−CS−Cu^{2+} increased (Figure 3A). Additionally, GSH concentration decreased as the treatment time increased, implying an effective depletion of GSH caused by PLNPs−CS−Cu^{2+} (Figure 3B). Therefore, the PLNPs−CS−Cu^{2+}-induced consumption of GSH could break the defense mechanism of bacteria and enhance the microbicidal efficacy.

$^{\bullet}$OH Generation. It is known that redox-active Cu^{2+} can be easily reduced to Cu^{+} by GSH, and the produced Cu^{+} can catalyze H_2O_2 to $^{\bullet}$OH *via* a Fenton-like reaction.[15,54] The cascade reactions are shown below

$$Cu^{2+} + GSH \rightarrow Cu^{+} + GSSG \quad (1)$$

$$Cu^{+} + H_2O_2 \rightarrow Cu^{2+} + {}^{\bullet}OH + OH^{-} \quad (2)$$

Thus, the Cu^{2+} in PLNPs−CS−Cu^{2+} could be reduced to Cu^{+} in PLNPs−CS−Cu^{+} by GSH. The change in the valence state was confirmed by XPS (Figure S6). The peaks of Cu $2p_{1/2}$ and Cu $2p_{3/2}$ slightly shifted from 952.1 and 932.5 eV to 951.9 and 932.3 eV, respectively, demonstrating the reduction of Cu^{2+} to Cu^{+}. Next, $^{\bullet}$OH generation was assessed by the methylene blue (MB) degradation approach. Figure 3C shows that the absorbance of MB at 663 nm had almost no change in the presence of PLNPs−CS−Cu^{+} or H_2O_2 only. In contrast, the absorbance of MB decreased significantly by introducing H_2O_2 into the mixture of MB and PLNPs−CS−Cu^{+}, indicating the generation of $^{\bullet}$OH. Figure S7 shows time-dependent degradation of MB. Furthermore, the generation of $^{\bullet}$OH was confirmed by electron spin resonance spectroscopy (EPR) using 5,5-dimethyl-1-pyridine N-oxide (DMPO) as the spin trap. Signals with a ratio of 1:2:2:1 proves the production of the $^{\bullet}$OH in the system (Figure 3D).

***In Vitro* Antibacterial Activity of PLNPs−CS−Cu^{2+}.** Inspired by the excellent properties of PLNPs−CS−Cu^{2+}, we examined the potential antimicrobial activity of PLNPs−CS−Cu^{2+} against Gram-positive *S. aureus* by the plate counting method. Different concentrations of H_2O_2 were incubated with bacteria; even 1 mM H_2O_2 had no obvious effect on bacterial activity (Figure S8). The incubation time was optimized, and 2 h was selected (Figure S9). The bacterial activity decreased as the concentration of PLNPs−CS−Cu^{2+} increased (Figure S10). As presented in Figure 4A,B, the similar colonies in PBS and H_2O_2 (1 mM) groups indicate that H_2O_2 alone had no obvious effect on *S. aureus* growth. The PLNPs−CS−Cu^{2+} (200 μg mL^{-1}) group exhibited weak antibacterial effects due to the presence of Cu^{2+}. In contrast, the PLNPs−CS−Cu^{2+} + H_2O_2 group yielded few colonies, confirming the CDT ability of PLNPs−CS−Cu^{2+} to catalyze the decomposition of H_2O_2 to $^{\bullet}$OH. Furthermore, the membrane integrity of bacteria was characterized *via* a live/dead staining assay. Live bacteria with an intact cell membrane could be stained with green fluorescence using Calcein acetoxymethyl ester (Calcein-AM), while dead bacteria with the damaged membrane would be stained with red fluorescence using propidium iodide (PI). Both PBS and H_2O_2 groups exhibited strong green fluorescence but almost no red fluorescence (Figure 4C), revealing that H_2O_2 alone had no

https://doi.org/10.1021/acsanm.3c00101
ACS Appl. Nano Mater. 2023, 6, 2274−2283

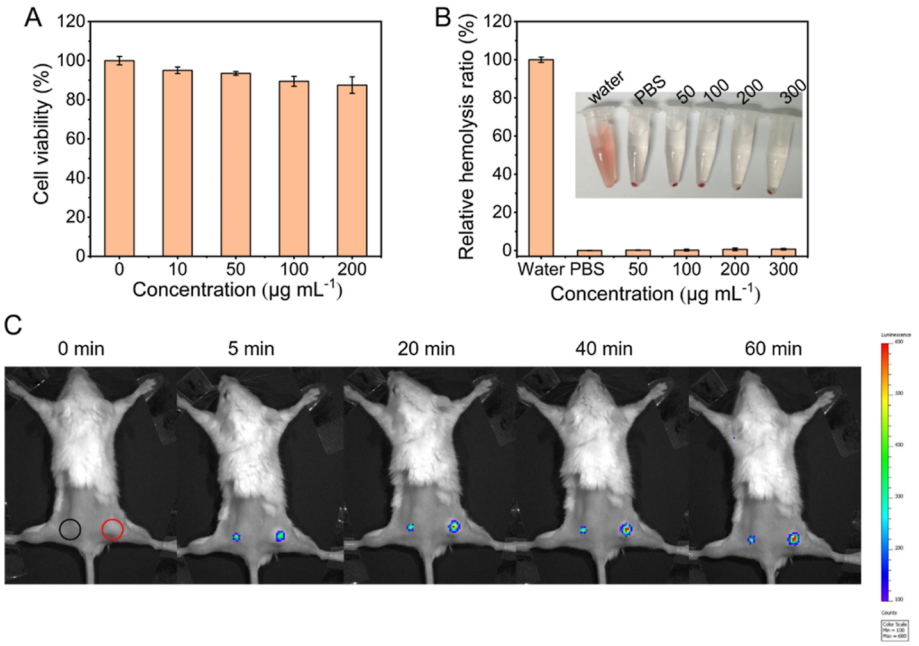

Figure 5. (A) Toxicity evaluation of PLNPs−CS−Cu^{2+} for 3T3 cells. Data were presented as the mean ± SD (n = 3). (B) Relative hemolysis ratio of water, PBS, and various concentrations of PLNPs−CS−Cu^{2+}. Data were presented as the mean ± SD (n = 3). (C) *In vivo* PL images of *S. aureus*-infected (red circle) and non-infected (black circle) areas of the same mice after subcutaneous injection of 200 μg mL^{-1} PLNPs−CS−Cu^{2+} (2 min 650 nm LED light illumination before each acquisition).

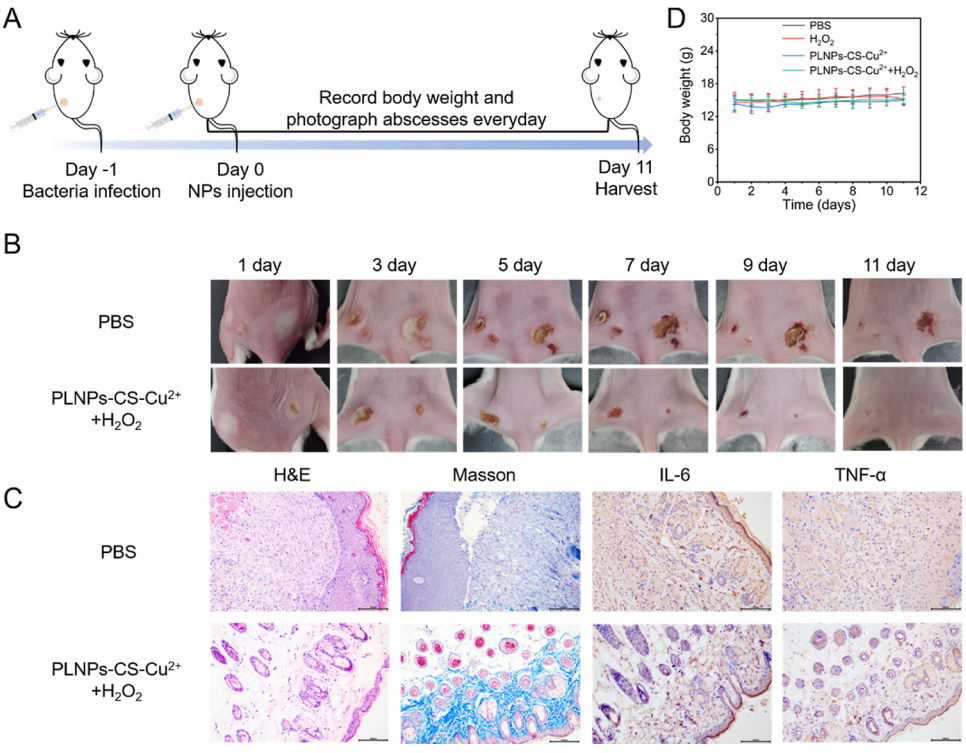

Figure 6. (A) Illustration for the building of the abscess model mice and the treatment process. (B) Photographs of the abscesses of the mice for 11 day treatment. (C) H&E, Masson staining, and immunohistochemical staining (including IL-6 and TNF-α) images of skin tissues on day 11 (scale bar, 100 μm). (D) Change in the body weight of mice in various treatment groups. Data were presented as the mean ± SD (n = 3).

significant effect on bacterial viability. Also, the PLNPs−CS−Cu^{2+} group exhibited weak red fluorescence signals, indicating the relatively weak antibacterial effect of Cu^{2+}. However, the PLNPs−CS−Cu^{2+} + H_2O_2 group induced strong red fluorescence, proving that apparently all of the bacterial cells were killed.

SEM was used to characterize the morphological change in bacteria (Figure 4D). The PBS group showed a smooth and intact bacterial surface. Co-incubation with H_2O_2 or PLNPs−CS−Cu^{2+} led to the slightly wrinkled surface of bacteria, indicating a minor impact on the integrity of bacterial cell membranes. In contrast, the PLNPs−CS−Cu^{2+} + H_2O_2 group

https://doi.org/10.1021/acsanm.3c00101
ACS Appl. Nano Mater. 2023, 6, 2274−2283

showed significant cellular deformation and leakage of the intracellular matrix, suggesting the strong antibacterial effect. In addition, the 2,7-dichlorofluorescin diacetate (DCFH-DA) probe was used to detect the $^{\bullet}OH$ in bacteria. Visibly stronger green fluorescence was observed in the PLNPs−CS−Cu^{2+} + H_2O_2 group, indicating the production of $^{\bullet}OH$ (Figure S11).

Toxicity Evaluation of PLNPs−CS−Cu^{2+}. Biocompatibility is crucial for *in vivo* antibacterial applications. Methylthiazolyl tetrazolium (MTT) assay of 3T3 cells was employed to examine the cytotoxicity of PLNPs−CS−Cu^{2+}. Figure 5A shows that the viability of 3T3 cells was still over 80% at 200 μg mL^{-1} PLNPs−CS−Cu^{2+}. Hemolysis experiment was also conducted to study the effect of PLNPs−CS−Cu^{2+} on red blood cells, and negligible hemolysis was observed at least up to 300 μg mL^{-1} PLNPs−CS−Cu^{2+} (Figure 5B). Thus, PLNPs−CS−Cu^{2+} possessed excellent biocompatibility and low long-term biotoxicity, which was suitable for *in vivo* treatment of bacterial infection.

***In Vivo* PL Imaging of Bacterial Infection.** To evaluate the *in vivo* imaging capability, PLNPs−CS−Cu^{2+} was subcutaneously injected on subcutaneously infected and non-infected areas of the same mouse. The NIR PL images of the mice were monitored over time after 2 min LED light illumination. Compared to non-infected areas, the subcutaneously infected areas showed a stronger NIR PL signal after 20 min post-injection (Figures 5C and S12). Moreover, the PL signal at the infected site was remarkably enhanced over time within 60 min. These results indicate that PLNPs−CS−Cu^{2+} has great potential for a real-time imaging with no auto-fluorescence and a high signal-to-noise ratio.

***In Vivo* Antibacterial Activity of PLNPs−CS−Cu^{2+}.** Considering the excellent bactericidal activity and biocompatibility of PLNPs−CS−Cu^{2+}*in vitro*, we further conducted *in vivo* antibacterial testing on *S. aureus*-infected mice (Figure 6A). The infected mice were randomly separated into four groups based on the used treatment agents: (1) PBS, (2) H_2O_2, (3) PLNPs−CS−Cu^{2+}, and (4) PLNPs−CS−Cu^{2+} + H_2O_2. Figures 6B and S13 showed the changes in mouse abscesses for 11 days. Compared to the PBS group, the abscess in the H_2O_2 and PLNPs−CS−Cu^{2+} group showed improved recovery, but a scab was still present. However, the infected site of the mice in the PLNPs−CS−Cu^{2+} + H_2O_2 group was gradually smoothing with the scars falling off. In addition, the abscess healing rate of the PLNPs−CS−Cu^{2+} + H_2O_2 group was also faster compared with other groups (Figure S14). To evaluate the antibacterial capability, the abscessed tissues were resected for bacterial counting (Figure S15). The colonies remarkably decreased in the PLNPs−CS−Cu^{2+} + H_2O_2 group, as demonstrated in *in vitro* antibacterial assay. The mice skin tissues were harvested at days 11 after infection. Hematoxylin−eosin (H&E), Masson staining, and immunohistochemistry staining were employed to evaluate the healing degree of the infected skin tissues (Figures 6C and S16). In the PBS group, a large number of inflammatory infiltrations were observed, while skin tissues obtained from the PLNPs−CS−Cu^{2+} + H_2O_2 treatment group showed fewer inflammatory cells, new hair follicles, and blood vessels. Masson staining showed an obvious increase in collagen deposition from the PLNPs−CS−Cu^{2+} + H_2O_2 group, indicating better tissue regeneration. Inflammation is a vital process during wound healing after the activation of inflammatory chemokines. The expression of proinflammatory cytokines such as interleukin-6 (IL-6) and tumor necrosis factor-α (TNF-α) was measured. The values of IL-6 and TNF-α significantly decreased in the PLNPs−CS−Cu^{2+} + H_2O_2 treatment group, revealing the reduction of bacterial infection. The weight of the mice from different treatment groups exhibited a similar increase (Figure 6D), suggesting negligible *in vivo* toxicity. The histological analysis results of major organs (spleen, heart, lung, liver, and kidney) exhibited no appreciable inflammatory lesion and injury after the whole treatment (Figure S17). The expulsion protocol of the material was demonstrated by *in situ* imaging. As the wound scabbed and fell off, the imaging signal almost disappeared (Figure S18). After 11 days of treatment, the mice were killed and organs were collected for imaging, and no obvious PL signal was found in the main organs of mice, proving the safety of the material (Figure S19). All of these results confirm that PLNPs−CS−Cu^{2+} is a promising therapeutic agent for antibacterial infection.

CONCLUSIONS

We have reported a facile fabrication of an infection microenvironment stimuli-responsive nanoplatform (PLNPs−CS−Cu^{2+}) for PL "turn-on" imaging and chemodynamic therapy of bacterial infection. The simple surface modification of PLNPs with CS and Cu^{2+} not only improved the biocompatibility but also exhibited the capability of chemodynamic antibacterial therapy stimulated by abnormally high GSH in the infection site. The integration of autofluorescence-free PL imaging ability into the antibacterial system enabled the developed nanoplatform to identify the lesion site and monitor the antibacterial process. *In vitro* experiment confirms that the nanoplatform has good biocompatibility and antibacterial activity. Furthermore, the PLNPs−CS−Cu^{2+} nanoplatform displays an obvious *in vivo* therapeutic effect on the abscess of the *S. aureus*-infected mice but with a negligible side effect on normal tissues or major organs. The developed infection microenvironment stimuli-responsive antibacterial strategy provides a feasible approach for the effective imaging and treatment of bacterial infection.

ASSOCIATED CONTENT

Supporting Information

The Supporting Information is available free of charge at https://pubs.acs.org/doi/10.1021/acsanm.3c00101.

Methods including materials and reagents, instrumentation and characterization, GSH-activated PL imaging, consumption of GSH, analysis of hydroxyl radical generation, live/dead staining analysis, morphological characterization of bacteria, detection of intracellular ROS, cell culture and *in vitro* cytotoxicity, hemolysis assay, statistics analysis, TEM images, size distribution, XRD patterns, excitation and emission spectra of PLNPs, XPS survey spectrum and stability of PLNPs−CS−Cu^{2+}, Cu 2p XPS spectrum of PLNPs−CS−Cu^{+}, UV−vis spectra of MB solution, effect of the concentration of H_2O_2 on bacterial viability, change in bacterial viability with incubation time, effect of the concentration of PLNPs−CS−Cu^{2+} on bacterial viability, analysis of $^{\bullet}OH$ generation in bacteria, radiance intensity obtained from persistent luminescence decay images for PLNPs−CS−Cu^{2+}*in vivo*, photographs of the abscesses of mice, relative abscess area of different groups, photographs and quantitative analysis of bacterial colonies, H&E, Masson staining, and immunohistochemical staining images, *in vivo* PL images of *S. aureus*-infected mice, and PL images of the mice main organs (PDF).

https://doi.org/10.1021/acsanm.3c00101
ACS Appl. Nano Mater. 2023, 6, 2274−2283

AUTHOR INFORMATION

Corresponding Author

Xiu-Ping Yan − *State Key Laboratory of Food Science and Technology, Jiangnan University, Wuxi 214122, China; International Joint Laboratory on Food Safety, Institute of Analytical Food Safety, School of Food Science and Technology, and Key Laboratory of Synthetic and Biological Colloids, Ministry of Education, Jiangnan University, Wuxi 214122, China;* orcid.org/0000-0001-9953-7681; Email: xpyan@jiangnan.edu.cn

Authors

Li-Ya Wang − *State Key Laboratory of Food Science and Technology, Jiangnan University, Wuxi 214122, China; International Joint Laboratory on Food Safety and Institute of Analytical Food Safety, School of Food Science and Technology, Jiangnan University, Wuxi 214122, China*

Li-Jian Chen − *State Key Laboratory of Food Science and Technology, Jiangnan University, Wuxi 214122, China; International Joint Laboratory on Food Safety and Institute of Analytical Food Safety, School of Food Science and Technology, Jiangnan University, Wuxi 214122, China;* orcid.org/0000-0001-8671-8766

Xu Zhao − *State Key Laboratory of Food Science and Technology, Jiangnan University, Wuxi 214122, China; International Joint Laboratory on Food Safety and Institute of Analytical Food Safety, School of Food Science and Technology, Jiangnan University, Wuxi 214122, China;* orcid.org/0000-0001-8000-9045

Yan Lv − *Key Laboratory of Synthetic and Biological Colloids, Ministry of Education and School of Chemical and Material Engineering, International Joint Research Laboratory for Nano Energy Composites, Jiangnan University, Wuxi 214122, China*

Tianxi Liu − *Key Laboratory of Synthetic and Biological Colloids, Ministry of Education and School of Chemical and Material Engineering, International Joint Research Laboratory for Nano Energy Composites, Jiangnan University, Wuxi 214122, China*

Complete contact information is available at: https://pubs.acs.org/10.1021/acsanm.3c00101

Notes

The authors declare no competing financial interest.

ACKNOWLEDGMENTS

This work was supported by the National Natural Science Foundation of China (no. 21934002), the National First-Class Discipline Program of Food Science and Technology (no. JUFSTR20180301), and the Collaborative Innovation Center of Food Safety and Quality Control in Jiangsu Province.

REFERENCES

(1) Willyard, C. The drug-resistant bacteria that pose the greatest health threats. *Nature* **2017**, *543*, 15.

(2) Wang, Y. X.; Li, S. L.; Liu, L. B.; Feng, L. H. Photothermal-responsive conjugated polymer nanoparticles for the rapid and effective killing of bacteria. *ACS Appl. Bio Mater.* **2018**, *1*, 27−32.

(3) Wang, Y.; Yang, Y. N.; Shi, Y. R.; Song, H.; Yu, C. Z. Antibiotic-free antibacterial strategies enabled by nanomaterials: progress and perspectives. *Adv. Mater.* **2020**, *32*, 1904106.

(4) Yan, S. Z.; Chen, S.; Gou, X. B.; Yang, J.; An, J. X.; Jin, X. Y.; Yang, Y. W.; Chen, L.; Gao, H. Biodegradable supramolecular materials based on cationic polyaspartamides and pillar[5]arene for targeting Gram-positive bacteria and mitigating antimicrobial resistance. *Adv. Funct. Mater.* **2019**, *29*, 1904683.

(5) Hwang, T. J.; Gibbs, K. A.; Podolsky, S. H.; Linder, J. A. Antimicrobial stewardship and public knowledge of antibiotics. *Lancet Infect. Dis.* **2015**, *15*, 1000−1001.

(6) Ma, W.; Chen, X. Y.; Fu, L. Q.; Zhu, J. W.; Fan, M. N.; Chen, J. P.; Yang, C.; Yang, G. Z.; Wu, L. H.; Mao, G. X.; Yang, X.; Mou, X. Z.; Gu, Z. W.; Cai, X. J. Ultra-efficient antibacterial system based on photodynamic therapy and CO gas therapy for synergistic antibacterial and ablation biofilms. *ACS Appl. Mater. Interfaces* **2020**, *12*, 22479−22491.

(7) Mei, L.; Lin, C. L.; Cao, F. Y.; Yang, D. H.; Jia, X.; Hu, S. J.; Miao, X. M.; Wu, P. F. Amino-functionalized graphene oxide for the capture and photothermal inhibition of bacteria. *ACS Appl. Nano Mater.* **2019**, *2*, 2902−2908.

(8) Zou, L. Y.; Hu, D. F.; Wang, F. J.; Jin, Q.; Ji, J. The relief of hypoxic microenvironment using an O_2 self-sufficient fluorinated nanoplatform for enhanced photodynamic eradication of bacterial biofilms. *Nano Res.* **2022**, *15*, 1636−1644.

(9) Pan, X. T.; Wu, N.; Tian, S. Y.; Guo, J.; Wang, C. H.; Sun, Y.; Huang, Z. Z.; Chen, F. Z.; Wu, Q. Y.; Jing, Y.; Yin, Z.; Zhao, B. H.; Xiong, X. L.; Liu, H. Y.; Zhou, D. S. Inhalable MOF-derived nanoparticles for sonodynamic therapy of bacterial pneumonia. *Adv. Funct. Mater.* **2022**, *32*, 2112145.

(10) Thakur, D.; Ta, Q. T. H.; Noh, J. S. Photosensitizer-conjugated hollow $ZnFe_2O_4$ nanoparticles for antibacterial near-infrared photodynamic therapy. *ACS Appl. Nano Mater.* **2021**, *5*, 1533−1541.

(11) Zhao, X.; Wei, X.; Chen, L. J.; Yan, X. P. Bacterial microenvironment-responsive dual-channel smart imaging-guided on-demand self-regulated photodynamic/chemodynamic synergistic sterilization and wound healing. *Biomater. Sci.* **2022**, *10*, 2907−2916.

(12) Lin, L. S.; Song, J. B.; Song, L.; Ke, K. M.; Liu, Y. J.; Zhou, Z. J.; Shen, Z. Y.; Li, J.; Yang, Z.; Tang, W.; Niu, G.; Yang, H. H.; Chen, X. Y. Simultaneous fenton-like ion delivery and glutathione depletion by MnO_2-based nanoagent to enhance chemodynamic therapy. *Angew. Chem., Int. Ed.* **2018**, *57*, 4902−4906.

(13) Zhang, S. N.; Lu, Q. J.; Wang, F. Y.; Xiao, Z. Y.; He, L. D.; He, D. G.; Deng, L. Gold-platinum nanodots with high-peroxidase-like activity and photothermal conversion efficiency for antibacterial therapy. *ACS Appl. Mater. Interfaces* **2021**, *13*, 37535−37544.

(14) Zhang, H. J.; Han, R. L.; Song, P. X.; Wei, X. J.; Hou, Y. F.; Yu, J. C.; Tang, K. Q. Hydrogen peroxide self-sufficient and glutathione-depleted nanoplatform for boosting chemodynamic therapy synergetic phototherapy. *J. Colloid Interface Sci.* **2023**, *629*, 103−113.

(15) Ma, B. J.; Wang, S.; Liu, F.; Zhang, S.; Duan, J. Z.; Li, Z.; Kong, Y.; Sang, Y. H.; Liu, H.; Bu, W. B.; Li, L. L. Self-assembled copper amino acid nanoparticles for in situ glutathione "AND" H_2O_2 sequentially triggered chemodynamic therapy. *J. Am. Chem. Soc.* **2019**, *141*, 849−857.

(16) Zhang, L.; Wan, S. S.; Li, C. X.; Xu, L.; Cheng, H.; Zhang, X. Z. An adenosine triphosphate-responsive autocatalytic fenton nanoparticle for tumor ablation with self-supplied H_2O_2 and acceleration of Fe(III)/Fe(II) conversion. *Nano Lett.* **2018**, *18*, 7609−7618.

(17) Yang, N.; Guo, H.; Cao, C. Y.; Wang, X. R.; Song, X. J.; Wang, W. J.; Yang, D. L.; Xi, L.; Mou, X. Z.; Dong, X. C. Infection microenvironment-activated nanoparticles for NIR-II photoacoustic imaging-guided photothermal/chemodynamic synergistic anti-infective therapy. *Biomaterials* **2021**, *275*, 120918.

(18) Qi, Ye.; Ren, S. S.; Ye, J. W.; Tian, Y. M.; Wang, G. Y.; Zhang, S. Q.; Du, L. Y.; Li, Y. C.; Che, Y.; Ning, G. L. Infection microenvironment-activated core-shell nanoassemblies for photothermal/chemodynamic synergistic wound therapy and multimodal imaging. *Acta Biomater.* **2022**, *143*, 445−458.

(19) Xu, Q. Q.; Hua, Y. S.; Zhang, Y. T.; Lv, M. Z.; Wang, H.; Pi, Y.; Xie, J. N.; Wang, C. Y.; Yong, Y. A Biofilm microenvironment-activated single-atom iron nanozyme with NIR-controllable nanocatalytic activities for synergetic bacteria-infected wound therapy. *Adv. Healthcare Mater.* **2021**, *10*, 2101374.

(20) Jia, C. Y.; Guo, Y. X.; Wu, F. G. Chemodynamic therapy via fenton and fenton-like nanomaterials: strategies and recent advances. *Small* **2022**, *18*, 2103868.
(21) Zheng, H.; Wang, S. Q.; Zhou, L.; He, X. J.; Cheng, Z. J.; Cheng, F.; Liu, Z.; Wang, X. Y.; Chen, Y. H.; Zhang, Q. Y. Injectable multi-responsive micelle/nanocomposite hybrid hydrogel for bioenzyme and photothermal augmented chemodynamic therapy of skin cancer and bacterial infection. *Chem. Eng. J.* **2021**, *404*, 126439.
(22) Liu, Y.; Wu, J. D.; Jin, Y. H.; Zhen, W. Y.; Wang, Y. H.; Liu, J. H.; Jin, L. H.; Zhang, S. T.; Zhao, Y.; Song, S. Y.; Yang, Y.; Zhang, H. J. Copper(I) phosphide nanocrystals for in situ self-generation magnetic resonance imaging-guided photothermal-enhanced chemodynamic synergetic therapy resisting deep-seated tumor. *Adv. Funct. Mater.* **2019**, *29*, 1904678.
(23) Ju, E. G.; Dong, K.; Chen, Z. W.; Liu, Z.; Liu, C. Q.; Huang, Y. Y.; Wang, Z. Z.; Pu, F.; Ren, J. S.; Qu, X. G. Copper(II)-graphitic carbon nitride triggered synergy: improved ROS generation and reduced glutathione levels for enhanced photodynamic therapy. *Angew. Chem., Int. Ed.* **2016**, *55*, 11467−11471.
(24) Zhang, W.; Lu, J.; Gao, X. N.; Li, P.; Zhang, W.; Ma, Y.; Wang, H.; Tang, B. Enhanced photodynamic therapy by reduced levels of intracellular glutathione obtained by employing a nano-MOF with Cu-II as the active center. *Angew. Chem., Int. Ed.* **2018**, *57*, 4891−4896.
(25) Sun, S.; Chen, Q.; Tang, Z. D.; Liu, C.; Li, Z. J.; Wu, A. G.; Lin, H. W. Tumor microenvironment stimuli-responsive fluorescence imaging and synergistic cancer therapy by carbon-dot-Cu^{2+} nanoassemblies. *Angew. Chem., Int. Ed.* **2020**, *59*, 21041−21048.
(26) Xiao, J. S.; Chen, S. Y.; Yi, J.; Zhang, H. F.; Ameer, G. A. A cooperative copper metal-organic framework-hydrogel system improves wound healing in diabetes. *Adv. Funct. Mater.* **2017**, *27*, 1604872.
(27) Gopal, A.; Kant, V.; Gopalakrishnan, A.; Tandan, S. K.; Kumar, D. Chitosan-based copper nanocomposite accelerates healing in excision wound model in rats. *Eur. J. Pharmacol.* **2014**, *731*, 8−19.
(28) Brewer, G. J. Risks of copper and iron toxicity during aging in humans. *Chem. Res. Toxicol.* **2010**, *23*, 319−326.
(29) Palza, H.; Nuñez, M.; Bastías, R.; Delgado, K. In situ antimicrobial behavior of materials with copper-based additives in a hospital environment. *Int. J. Antimicrob. Agents* **2018**, *51*, 912−917.
(30) Arjunan, N.; Singaravelu, C. M.; Kulanthaivel, J.; Kandasamy, J. A potential photocatalytic, antimicrobial and anticancer activity of chitosan-copper nanocomposite. *Int. J. Biol. Macromol.* **2017**, *104*, 1774−1782.
(31) Sun, X. Y.; Dong, M. N.; Guo, Z. R.; Zhang, H.; Wang, J.; Jia, P.; Bu, T.; Liu, Y. N.; Li, L. H.; Wang, L. Multifunctional chitosan-copper-gallic acid based antibacterial nanocomposite wound dressing. *Int. J. Biol. Macromol.* **2021**, *167*, 10−22.
(32) Guibal, E.; Vincent, T.; Navarro, R. Metal ion biosorption on chitosan for the synthesis of advanced materials. *J. Mater. Sci.* **2014**, *49*, 5505−5518.
(33) Wang, G. Y.; Ye, J. W.; Wang, M.; Qi, Y.; Zhang, S. Q.; Shi, L.; Fang, Y. G.; Tian, Y. M.; Ning, G. L. Copper boron-imidazolate framework incorporated chitosan membranes for bacterial-infected wound healing dressing. *Carbohydr. Polym.* **2022**, *291*, 119588.
(34) Brunel, F.; El Gueddari, N. E.; Moerschbacher, B. M. Complexation of copper(II) with chitosan nanogels: toward control of microbial growth. *Carbohydr. Polym.* **2013**, *92*, 1348−1356.
(35) Wang, X. H.; Du, Y. M.; Fan, L. H.; Liu, H.; Hu, Y. Chitosan-metal complexes as antimicrobial agent: synthesis, characterization and structure-activity study. *Polym. Bull.* **2005**, *55*, 105−113.
(36) Liu, D. H.; Zhou, Z. J.; Wang, X. Y.; Deng, H. Z.; Sun, L.; Lin, H. X.; Kang, F.; Zhang, Y.; Wang, Z. T.; Yang, W. J.; Rao, L.; Yang, K. K.; Yu, G. C.; Du, J. S.; Shen, Z. Y.; Chen, X. Y. Yolk-shell nanovesicles endow glutathione-responsive concurrent drug release and T_1 MRI activation for cancer theranostics. *Biomaterials* **2020**, *244*, 119979.
(37) Yuwen, L. H.; Qiu, Q.; Xiu, W. J.; Yang, K. L.; Li, Y. Q.; Xiao, H.; Yang, W. J.; Yang, D. L.; Wang, L. H. Hyaluronidase-responsive phototheranostic nanoagents for fluorescence imaging and photothermal/photodynamic therapy of methicillin-resistant Staphylococcus aureus infections. *Biomater. Sci.* **2021**, *9*, 4484−4495.
(38) Xu, L. T.; Zhou, K.; Ma, H. L.; Lv, A. Q.; Pei, D. D.; Li, G. P.; Zhang, Y. F.; An, Z. F.; Li, A.; He, G. Ultralong organic phosphorescent nanocrystals with long-lived triplet excited states for afterglow imaging and photodynamic therapy. *ACS Appl. Mater. Interfaces* **2020**, *12*, 18385−18394.
(39) Abdukayum, A.; Chen, J. T.; Zhao, Q.; Yan, X. P. Functional near infrared-emitting Cr^{3+}/Pr^{3+} Co-doped zinc gallogermanate persistent luminescent nanoparticles with superlong afterglow for in vivo targeted bioimaging. *J. Am. Chem. Soc.* **2013**, *135*, 14125−14133.
(40) Wu, B. Y.; Wang, H. F.; Chen, J. T.; Yan, X. P. Fluorescence resonance energy transfer inhibition assay for α-fetoprotein excreted during cancer cell growth using functionalized persistent luminescence nanoparticles. *J. Am. Chem. Soc.* **2011**, *133*, 686−688.
(41) Teston, E.; Maldiney, T.; Marangon, I.; Volatron, J.; Lalatonne, Y.; Motte, L.; Boisson-Vidal, C.; Autret, G.; Clément, O.; Scherman, D.; Gazeau, F.; Richard, C. Nanohybrids with magnetic and persistent luminescence properties for cell labeling, tracking, in vivo real-time imaging, and magnetic vectorization. *Small* **2018**, *14*, 1800020.
(42) Yan, L. X.; Chen, L. J.; Zhao, X.; Yan, X. P. pH switchable nanoplatform for in vivo persistent luminescence imaging and precise photothermal therapy of bacterial infection. *Adv. Funct. Mater.* **2020**, *30*, 1909042.
(43) Wang, B. B.; Yan, L. X.; Chen, L. J.; Zhao, X.; Yan, X. P. Responsive nanoplatform for persistent luminescence "turn-on" imaging and "on-demand" synergistic therapy of bacterial infection. *J. Colloid Interface Sci.* **2022**, *610*, 687−697.
(44) Chen, L. J.; Zhao, X.; Yan, X. P. Cell-penetrating peptide-functionalized persistent luminescence nanoparticles for tracking J774A.1 macrophages homing to inflamed tissues. *ACS Appl. Mater. Interfaces* **2019**, *11*, 19894−19901.
(45) Feng, Y.; Zhang, L. C.; Liu, R.; Lv, Y. Modulating near-infrared persistent luminescence of core-shell nanoplatform for imaging of glutathione in tumor mouse model. *Biosens. Bioelectron.* **2019**, *144*, 111671.
(46) Li, Y. J.; Yan, X. P. Synthesis of functionalized triple-doped zinc gallogermanate nanoparticles with superlong near-infrared persistent luminescence for long-term orally administrated bioimaging. *Nanoscale* **2016**, *8*, 14965−14970.
(47) Zhang, X. Z.; Zhang, C.; Shu, Q. M.; Xu, C.; Zheng, Q. Q.; Guo, Z.; Wang, C.; Hao, Z. X.; Liu, X.; Wang, G. Q.; Yan, W. J.; Chen, H. P.; Lu, C. Y. Copper clusters: an effective antibacterial for eradicating multidrug-resistant bacterial infection in vitro and in vivo. *Adv. Funct. Mater.* **2021**, *31*, 2008720.
(48) Zhou, X.; Zhang, S.; Liu, Y.; Meng, J. S.; Wang, M. X.; Sun, Y. J.; Xia, L. B.; He, Z. Z.; Hu, W. X.; Ren, L.; Chen, Z. W.; Zhang, X. C. Antibacterial cascade catalytic glutathione-depleting MOF nanoreactors. *ACS Appl. Mater. Interfaces* **2022**, *14*, 11104−11115.
(49) Xu, M. R.; Hu, Y.; Xiao, Y.; Zhang, Y. Y.; Sun, K. L.; Wu, T.; Lv, N.; Wang, W. S.; Ding, W. P.; Li, F. F.; Qiu, B. S.; Li, J. B. Near-infrared-controlled nanoplatform exploiting photothermal promotion of peroxidase-like and OXD-like activities for potent antibacterial and anti-biofilm therapies. *ACS Appl. Mater. Interfaces* **2020**, *12*, 50260−50274.
(50) Ding, M.; Zhao, W.; Song, L. J.; Luan, S. F. Stimuli-responsive nanocarriers for bacterial biofilm treatment. *Rare Met.* **2022**, *41*, 482−498.
(51) Teston, E.; Lalatonne, Y.; Elgrabli, D.; Autret, G.; Motte, L.; Gazeau, F.; Scherman, D.; Clément, O.; Richard, C.; Maldiney, T. Design, properties, and in vivo behavior of superparamagnetic persistent luminescence nanohybrids. *Small* **2015**, *11*, 2696−2704.
(52) Li, T. L.; Zhou, J.; Wang, L. R.; Zhang, H. F.; Song, C. F.; de la Fuente, J. M.; Pan, Y. X.; Song, J.; Zhang, C. L.; Cui, D. X. Photo-fenton-like metal-protein self-assemblies as multifunctional tumor theranostic agent. *Adv. Healthcare Mater.* **2019**, *8*, 1900192.
(53) Xiao, J. Y.; Hai, L.; Li, Y. Y.; Li, H.; Gong, M. H.; Wang, Z. F.; Tang, Z. F.; Deng, L.; He, D. G. An ultrasmall Fe_3O_4-decorated polydopamine hybrid nanozyme enables continuous conversion of

https://doi.org/10.1021/acsanm.3c00101
ACS Appl. Nano Mater. 2023, 6, 2274−2283

oxygen into toxic hydroxyl radical via GSH-depleted cascade redox reactions for intensive wound disinfection. *Small* **2022**, *18*, 2105465.
(54) Guo, W. T.; Ji, T. X.; Deng, Y. H.; Liu, J.; Gou, Y. T.; Dong, W. K. Facile synthesis of a glutathione-depleting Cu(II)-half-salamo-based coordination polymer for enhanced chemodynamic therapy. *Dalton Trans.* **2022**, *51*, 11884−11891.

NOTE ADDED AFTER ASAP PUBLICATION

This paper was published on January 26, 2023. Due to production error, equations 1 and 2 were rendered incorrectly. The corrected version was reposted on January 27, 2023.

https://doi.org/10.1021/acsanm.3c00101
ACS Appl. Nano Mater. 2023, 6, 2274−2283